Article

316L(N) Creep Modeling with Phenomenological Approach and Artificial Intelligence Based Methods

Daniele Baraldi [1,*], Stefan Holmström [2], Karl-Fredrik Nilsson [1], Matthias Bruchhausen [1] and Igor Simonovski [1]

[1] European Commission, Joint Research Centre (JRC), 1755 LE Petten, The Netherlands;
Karl-Fredrik.NILSSON@ec.europa.eu (K.-F.N.); Matthias.BRUCHHAUSEN@ec.europa.eu (M.B.);
Igor.SIMONOVSKI@ec.europa.eu (I.S.)
[2] SCK-CEN, Belgian Nuclear Research Centre, 2400 Mol, Belgium; stefan.holmstrom@sckcen.be
* Correspondence: Daniele.BARALDI@ec.europa.eu; Tel.: +31-(0)224-56-5140

Abstract: A model that describes creep behavior is essential in the design or life assessment of components and systems that operate at high temperatures. Using the RCC-MRx data and the LCSP (logistic creep strain prediction) model, processed design data were generated over the whole creep regime of 316L(N) steel—i.e., primary, secondary, and tertiary creep. The processed design data were used to develop three models with different approaches for the creep rate: a phenomenological approach; an artificial neural network; and an artificial intelligence method based on symbolic regression and genetic programming. It was shown that all three models are capable of describing the true creep rate as a function of true creep strain and true stress over a wide range of engineering stresses and temperatures without the need of additional micro-structural information. Furthermore, the results of finite element simulations reproduce the trends of experimental data from the literature.

1. Introduction

For structures operating at high temperature conditions, creep phenomena are one of the main failure mechanisms that can jeopardize the structural integrity of a component and the full system. Therefore, the accurate prediction of the creep behavior is essential in both the design and operational stages to ensure the structural integrity of components during their entire life.

The creep deformation typically has three stages: the primary creep stage, where the strain rate decreases with time; the secondary creep stage with a constant strain rate; and the tertiary creep stage where the strain rate increases prior to rupture. Components, in nuclear reactors for instance are designed so that accumulated creep strains remain small through the entire life and therefore only primary and secondary creep are relevant. For end-of-life assessment on the other hand, where the objective is to demonstrate margins to failure, secondary and tertiary creep are of interest. Tertiary creep may also be needed to assess margins against failure of components in more extreme accident situations resulting in temperature or stress surges. Thus, for a full creep assessment, a creep model that includes all creep stages is needed. Engineering creep models are typically limited to one or two of the creep stages [1] and only a few models exist that describe the entire creep life. These include the modified Garofalo model, a design creep model extended by tertiary creep [2] and the modified omega model, where secondary and tertiary creep are extended by primary creep [3]. More mechanistic constitutive models have also been proposed that account for different deformation and damage mechanisms but require additional microstructural data [4–6]. Any creep model needs to have its parameters fitted to data. The larger the range in terms of stress and temperature, the more difficult the fitting becomes and creep models are therefore often limited to relatively narrow ranges.

This problem is exacerbated when the complexity of the model increases. Moreover, for calibration, the handling of scatter in the material data is also a challenge.

A third complication is that creep and plastic deformation occur simultaneously during a standard creep test. A test specimen may be plastically deformed at the start-up of the creep test. Furthermore, if the creep rupture is ductile it will be a combination of plastic collapse and creep rupture. Uniaxial creep tests measure the total deformation so it is not possible to distinguish between 'true' creep and increasing plastic deformation due to increasing true stress. The plasticity effect depends obviously on the load but also on the material and can be quite significant for austenitic steels. However, a constitutive model must account for both plasticity and creep.

The objective of this work is to develop analytical models that describe the creep behavior from initial loading to component failure, including plasticity effects, and that can be used in FE codes such as Abaqus for numerical simulations of relevant creep phenomena. The definition of the material creep properties as inputs to FE codes is based on the true values rather than the engineering values, as large strains need to be taken into account for creep rupture. In fact, the accelerated creep deformation at rupture is caused more by plastic collapse triggered by the increasing true stress than creep damage. Therefore, in this paper we develop a true stress-strain constitutive model for the plastic hardening calibrated to tensile tests and models for true creep rate as a function of true creep strain, true stress, and temperature. The material selected for this study is the austenitic stainless steel 316L(N) since that material is used, or envisaged to be used, for both conventional and nuclear power plants and in the International Nuclear Fusion Project. Nevertheless, the procedure in this study can be applied to other materials.

2. Methods and Models

One of the main issues in the development of a creep model is to identify a set of creep data covering a wide range of temperatures and stress levels. According to the authors' knowledge, a set of experimental data over a large span of conditions is not available in the scientific literature, especially for low creep rates (low temperature or low stress) and very large rupture times (>100,000 h).

Given the wide range of conditions defined in the code, RCC-MRx [7] has been selected as the source for the required data. RCC-MRx covers consistently the design and construction of components for high temperature, research, and fusion reactors [8–12]. In RCC-MRx, separate analytical expressions are provided for the primary and secondary creep regimes. The only information available in the code related to the tertiary creep is the table of the rupture strength. The RCC-MRx equations for creep strain and creep strain rate covering the primary and secondary creep regime are themselves models and the creep rupture strength tables are also based on models. Both model types were optimized on an undisclosed set of raw data. Nevertheless, RCC-MRx is considered to give a representative and coherent set of engineering data. The resulting enhanced and coupled creep strain models from this work are therefore expected to depict code compliant (average) creep deformation properties in the true stress–temperature–time space assessed here.

RCC-MRx is also used as a data source to develop a constitutive model for the 316L(N) elasto-plastic properties in Section 2.1. In Section 2.2.1, the logistic creep strain prediction (LCSP) model [13–15] has been used to couple the RCC-MRx data to describe in full the three creep stages, including the transition between the different stages and the final creep rupture. By means of the LCSP model, the engineering strain vs. time data are generated for each temperature and for each engineering stress.

By means of the elasto-plastic constitutive model, the true creep rate is calculated as a function of true creep strain and true stress as explained in Section 2.2.2. The outcome of the above procedure is one set of data in terms of true creep rate, true creep strain, and true stress for each engineering stress and temperature. Those data are referred to as 'processed design data' hereafter.

In Section 3, the processed design data have been used to develop analytical expressions for the true creep rate by means of three different approaches: a phenomenological approach and two methods based on artificial intelligence.

Finally, a comparison between the FE simulation results and a set of experimental data from the literature [16] is performed in Section 4. The full procedure that has been followed in this research is shown in Figure 1.
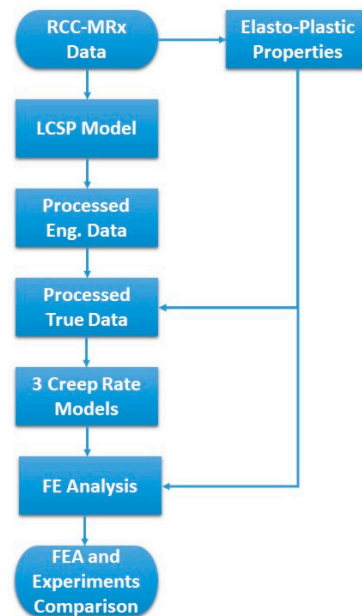
Figure 1. Flow chart with the layout of the content of the paper.

2.1. Elasto-Plastic Constitutive Model

The 316L(N) engineering tensile properties for the stress and the strain are derived from the RCC-MRx code [A3.1S.451 and A3.1S.452] and converted into true values

$$\varepsilon_t = \ln(1 + e_t); \ \sigma_t = R\,(1 + e_t) \tag{1}$$

The following analytical expression with a yield stress, one linear term and two non-linear isotropic hardening terms is used for fitting the true stresses σ_t versus the true plastic strains ε_p

$$\sigma_t = P_{R0} + P_H\varepsilon_p + P_{Q1}\left[1 - \exp\left(-P_{b1}\varepsilon_p\right)\right] + P_{Q2}\left[1 - \exp\left(-P_{b2}\varepsilon_p\right)\right] \tag{2}$$

The parameters P_{R0}, P_H, P_{Q1}, P_{Q2}, P_{b1}, and P_{b2} in Equation (2) are fitted to the RCC-MRx data and are included in Table 1. The resulting tensile responses for temperatures equal to 600 °C, 650 °C, and 700 °C are shown in Figure 2.

Table 1. Young modulus and parameters for Equation (2) at T = 600 °C, 650 °C, and 700 °C

T (°C)	E (GPa)	P_{R0} (MPa)	P_H (MPa)	P_{Q1} (MPa)	P_{b1}	P_{Q2} (MPa)	P_{b2}
700	142.3	89.74	336.4	158.2	30.64	30.798	2544.68
650	146.54	93.24	392.5	242.24	17.49	32.05	2086.23
600	150.78	97.47	374.91	298.14	11.49	33.79	1335.28

In the RCC-MRx code material properties are not provided for larger strains (>30%) and the authors could not find material data in the literature to describe the 316L(N) behavior at high temperatures for those large strains. Therefore, the fitting for Equation (2) is based on interpolation in the strain range where RCC-MRx data are available, and

this function is then used for extrapolation to larger strains where data are not available as shown in Figure 2. Although the extrapolation procedure introduces uncertainties in the models, it will be shown in Section 4 that the overall model's performance is satisfactory in reproducing the processed RCC-MRx data.
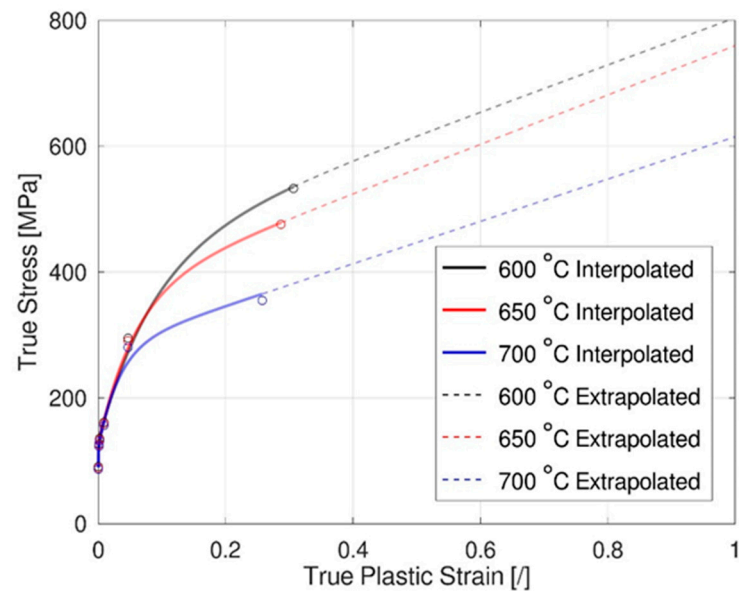
Figure 2. True stress vs. true plastic strain at 600 °C, 650 °C, and 700 °C. Circles for the RCC-MRX data and line for the fitted Equation (2). Continuous line for interpolated values and dashed line for extrapolated values.

2.2. 'Processed' Design Data

2.2.1. Processed Engineering Data—LCSP Model

In this work, full creep strain curves, including primary, secondary and tertiary are derived from the material properties of RCC-MRx using the logistic creep strain prediction (LCSP) model [13–15]. To accomplish this, the models from the design code defined for primary and secondary creep strain are coupled to the creep strength properties, also given in the code. Since RCC-MRx only provides formulations for the primary and secondary creep regime, the tertiary creep strain part included here cannot be claimed to be compliant with the code. However, by coupling the RCC-MRx strain model with the corresponding rupture strength table, the acquired full creep curves are considered good representations of the material behavior.

In RCC-MRx (A3.1S.53b creep strength table), the average values of the creep rupture stress are tabulated as a function of temperature, including the temperatures used in this work, and as a function of time, ranging from 1 h to 3×10^5 h. In the RCC-MRx creep strength table, the values of the rupture stress are provided in the following ranges: from 118 MPa to 351 MPa for 600 °C, from 75 to 298 MPa for 650 °C, and from 57 to 257 MPa for 700 °C. The values of creep rupture stress, creep rupture time t_u, and temperature T from the table are used to generate the end point of each 'processed' creep strain curve generated for this work.

The primary creep stage of the processed creep strain curves is acquired at specified temperature and engineering stress using the RCC-MRx equations for the average creep strain e_f at the specified time; the end of primary creep time t_{fp}; the average (engineering) strain at the end of primary creep e_{ffp}; and the average (engineering) primary creep strain rate $\dot{e}_{fp}$. For the secondary creep strain regime, the average strain rate $\dot{e}_s$ is taken from the end of primary creep stage ($e_f > e_{ffp}$). The stress values at the minimum creep rate are given as a function of temperature in the RCC-MRx table A3.1S.542 for the time range between 100 h and 3×10^5 h. The table sets the time-stress conditions at the end of the

secondary creep, noting that the tertiary creep, later enhanced by necking beyond A_g, has not yet started. Thus, the stress range in this table can be considered a representative range where the RCC-MRx strain equations can be applied with confidence. The values of this table were modeled using the Larson–Miller time–temperature parameter [17] to give an estimate of the location in the time–strain creep curve where the secondary creep regime is expected to end and the tertiary regime to begin. These curve-specific estimates were used as a quality check but were not taken into account in the final fitting of the full strain curve. Although this was attempted, at the shorter times below 100 h (outside the table range) the coupling between rupture time and end of secondary creep did not give satisfactory results since in some cases the predicted time to end of secondary was larger than time to rupture. Also, the time to the end of primary creep and time to rupture did not match well, i.e., $t_{pf} > t_u$ for the largest stresses at the lower temperatures (650 °C and 600 °C). In these cases, the modeling of the coupled creep curve was conducted by extending the time to rupture by a factor, placing the end of primary in a 'credible' time fraction of about 10–20% in time. At very high stresses, in or close to 'power law breakdown', where considerable initial plastic deformation is unavoidable, the distinction between classical 'creep strain' and the initial 'plastic deformation' is in many cases left to the scrutiny of the creep data assessor.

The LCSP model [13–15] has been used here to describe the three creep stages (primary, secondary, and tertiary) in full, including the transitions between the different stages and the final creep rupture. The LCSP model was previously successfully used to investigate creep phenomena in final repository copper canisters [18] and in fuel cladding [19]. The model was developed further to include the creep-fatigue interactions [20] and in recent years the model was used for life-extension studies [21,22]. As described above, the processed curves generated for this work use the LCSP model to fit the RCC-MRx defined primary and secondary creep ranges coupled with the average creep rupture properties.

The LSCP creep model is based on the expressions

$$\log(t_e) = \frac{[\log(t_u) + C]}{1 + [\log(e)/x_0]^p} - C, \quad \log(e_t) = \left[\frac{\log(t_u) + C}{\log(t_e) + C} - 1\right]^{1/p} x_0 \qquad (3)$$

where t_e is the time to the given engineering strain e, t_u is the time to rupture, and x_0 and p are fitting parameters. C is a Larson-Miller type parameter, which identifies the minimum time that can be predicted by the model as 10^{-C} hours. Apart from defining the shortest time of the model applicability, the C parameter has a limited effect on the LCSP fit of the data. The p and x_0 parameters require an optimization for each condition of time to rupture, temperature, and engineering stress. The optimal values of x_0 and p as a function of stress, temperature, strain at minimum creep rate, etc. can be found to create a generic creep strain model but this is not a topic of this paper.

As briefly described above, the LCSP model is fitted to the RCC-MRx primary creep strain curves up to the end of the primary creep time t_{fp}, reaching the RCC-MRx minimum creep rate at that time and the final rupture point at time to rupture t_u. In Figure 3, an example of the outcome of the fitting procedure for the case with engineering stress of 171 MPa and 650 °C is shown. The RCC-MRx creep strain curve (with only the primary and secondary creep stages) and the corresponding LCSP curve are plotted, covering the complete creep range, including the tertiary creep.

Note that for the full 'processed' LCSP creep curves used in the further calibration of the Abaqus/Zmat constitutive equations are the best fits for each condition. For each temperature, stress, and time to rupture condition, x_0 and p have been optimized for a constant value of $C = 4$. The 'best fit' is obtained when the minimum root mean square of the logarithmic strain in the primary-creep region is obtained with the anchoring end set at time to rupture t_u. The acquired optimal x_0 and p values for the test conditions of this work are given in Appendix A.
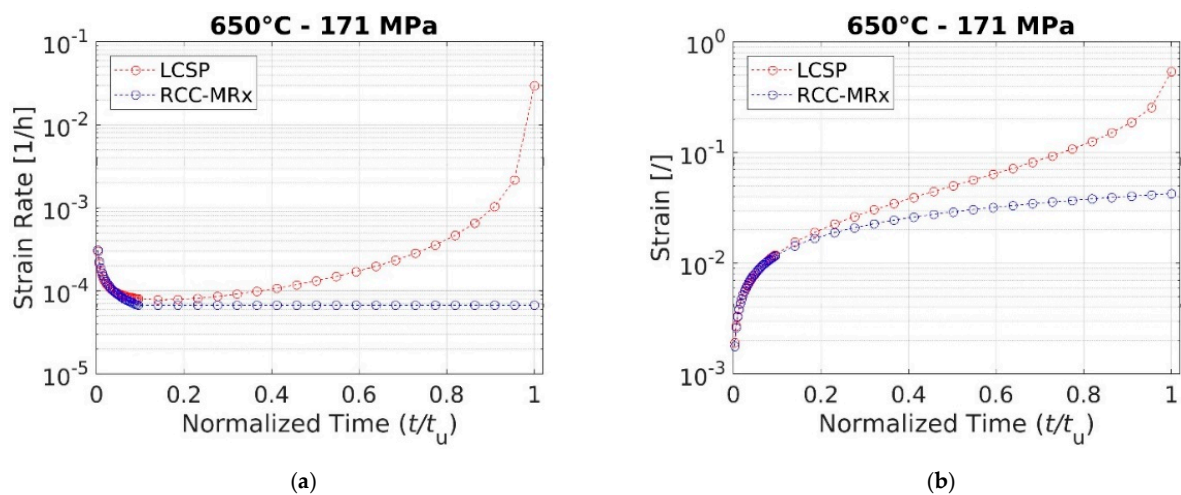
Figure 3. T = 650 °C, t_u = 1000 h and engineering stress = 171 MPa. (**a**) engineering creep strain rate strain vs. normalized time and (**b**) engineering creep strain rate strain vs. normalized time for an RCC-MRx calculated primary–secondary creep curve and the corresponding LCSP curve.

It must be emphasized that stresses and strains are engineering values both in the LCSP model and in the RCC-MRx tables and models.

It must also be noted that for the tertiary creep, the RCC-MRx provides only the rupture times and stresses; whereas for the primary and secondary, it provides the complete and detailed material properties for the creep curve. Therefore, it can be expected that uncertainties in the LCSP generated creep curves are larger in the tertiary creep than in the primary and secondary one.

2.2.2. Processed True Data

The time and the engineering creep strain from Equation (3) are used to define the true values of the creep strain rate as function of the true stress, and the true creep strain in the following stages. As customary in experimental tests, it is assumed that the engineering creep strain is the total engineering strain under constant load, i.e., the actual creep strain and the increase in plastic strain with increasing true stress. Furthermore, it is also assumed that the total strain is composed of three separate parts: a time-independent elastic part, a time-independent plastic part, and a time-dependent creep part.

Given the engineering strain increment under constant load $\Delta e(t)$ recorded for the specific time increment Δt, the following steps are implemented to define the true creep strain rate $\dot{\varepsilon}_f(t)$, the true stress $\sigma(t)$, and the true creep strain $\varepsilon_f(t)$:

1. The initial engineering strain, $e(0)$ is computed as the sum of the initial elastic part (which can be calculated by means of the Young's modulus from the initial stress) and of the initial plastic part (which can be from the tensile model). The creep component is not considered in the initial engineering strain.
2. The total engineering strain, $e(t)$ is calculated as the sum of two quantities: the initial engineering strain, $e(0)$ and the engineering strain increment, $de(t)$: $e(t) = e(0) + de(t)$;
3. The true stress and the total true strain are calculated using Equation (1);
4. The true elastic stress is calculated as $\varepsilon_e(t) = \sigma_t(t)/E$;
5. The true plastic strain $\varepsilon_p(t)$ is calculated as $\varepsilon_p(t) = \varepsilon_t(t) - \sigma_t(t)/E$.
6. The 'true' creep strain is calculated by subtracting the elastic and plastic parts from the total strain $\varepsilon_f(t) = \varepsilon_t(t) - \varepsilon_e(t) - \varepsilon_p(t)$.
7. The creep strain rate is calculated as the differentiation of the creep strains with respect to time: $\dot{\varepsilon}_f(t) = d\varepsilon_f(t)/dt$.

Since the procedure is repeated for each recorded strain increment, the elastic, plastic and creep contributions are also recorded. The separation is based on the assumption that the elasto-plastic stress–strain curve is not affected by the creep deformation.

The true creep strain rate, $\dot{\varepsilon}_f(t)$, the true stress, $\sigma(t)$, and the true creep strain, $\varepsilon_f(t)$ from the above procedure, are used to calibrate three creep models with different approaches: a phenomenological approach, and two approaches based on artificial intelligence.

The processed data for the true creep rate are represented in Figure 4.
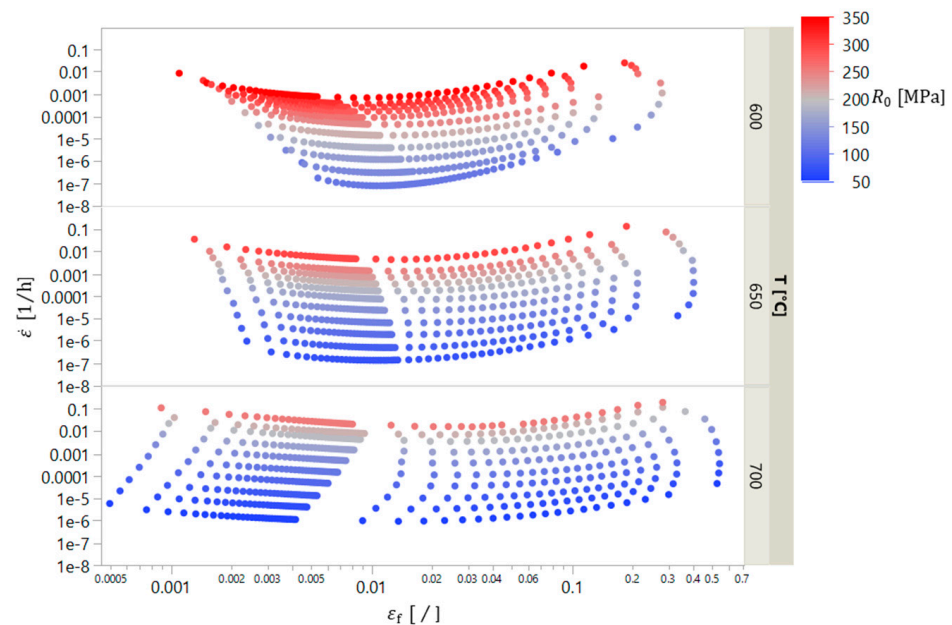
Figure 4. Processed dataset for the creep rates.

2.3. Creep Rate Models

In the previous section, processed true data have been determined over a wide range of temperatures and engineering stresses, using RCC-MRx as the source for the initial engineering data. In this section, three creep rate models are developed based on the processed data.

The first model is based on a parametrized equation describing the creep rates with a pre-defined form that accounts from primary to tertiary creep. The other two models are based on artificial intelligence algorithms. The second model is based on a neural network that uses the hyperbolic tangent as an activation function to describe the creep rate. Also for the second model, the form of the analytical expression for the creep rate is defined from the beginning, at least partly. The third model is based on a symbolic regression method, which searches for both the parameters and the form of the equation simultaneously. The three models are referred to as PA (phenomenological approach) model, NN (neural network) model, and SR (symbolic regression) model hereafter.

To the authors' knowledge, this is the first time that symbolic regression is applied to 316L(N) creep modeling and few studies based on the application of artificial neural network to same topic were performed [23,24].

One of the issues with complex models like those that are developed with artificial intelligence (such as the NN and SR models) is overfitting. Overfitting can occur when a model has too many parameters and follows the data too closely. The most useful model, i.e., the model that best describes the trend of the data is not necessarily the model that gives the best fit of the data. As a measure to detect the potential for overfitting, the processed data set (1600 points) has been randomly split in a training set (two-thirds of the data) and a validation set (one-third of the data). Figure 5 shows the training and validation data for 650 °C as an example. Figure 6 shows the repartition of the training and validation sets over the three independent variables T, ε_f, and $\dot{\varepsilon}_f$. The training set is used for determining the model parameter whereas the validation set serves to select the most useful model. If a model describes the training set significantly better than the validation set, this in an indication that the model may over-fit.
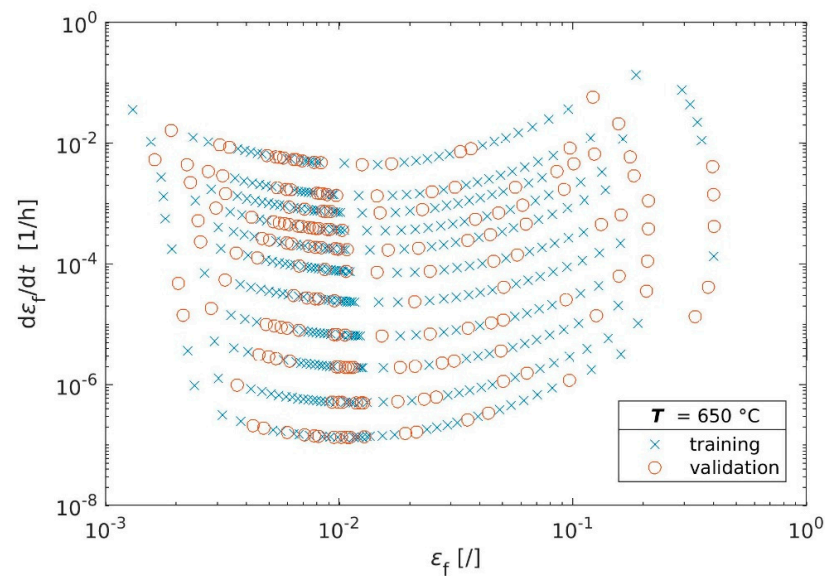
Figure 5. Split of the data in a training and a validation set (data at 650 °C).
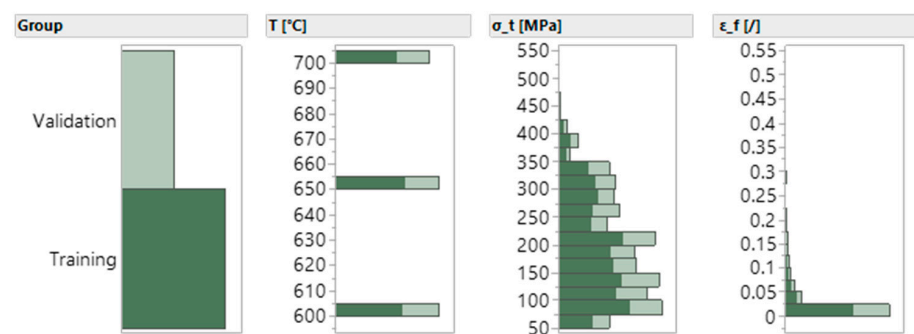

Figure 6. Distribution of the validation and training sets for the three independent variables.

To ensure comparability between the two AI models, the same split between training and validation set was used for both methods. The phenomenological approach is based on a relatively simple analytical expression with a limited number of parameters. Therefore, it was not deemed necessary to carry out the same overfitting analysis as for the two AI models. Moreover, in the 'Results' section, all the models will be successfully applied in FEA for engineering stresses that are not included in the calibration data, providing a further confirmation that over-fitting does not occur.

2.3.1. Phenomenological Approach Model (PA)

In the phenomenological approach, it is assumed that the creep rate, $\dot{\varepsilon}_f(t)$ is a function with a pre-defined form which depends on the true creep strain, $\varepsilon_f(t)$ and the true stress, $\sigma(t)$

$$\dot{\varepsilon}_f(t) = \left\{ \frac{\sigma(t)}{K_0 + K_1\left[1 - exp\left(-b_1\varepsilon_f(t)\right)\right] - K_2\left[1 - exp\left(-b_2\varepsilon_f(t)\right)\right]} \right\}^{n_{Nort}} \tag{4}$$

If K_1 and K_2 are zero, the model reduces to a standard Norton creep model. Assuming K_1 and K_2 to be positive, the exponential terms correspond to primary and tertiary creep respectively and b_1 and b_2 are the corresponding creep rates. The five fitting parameters K_0, K_1, K_2, b_1, and b_2 are calibrated with a two-step optimization procedure. In the first step, different sets of the five parameters are identified for each engineering stress. The Octave lsqcurvefit function is used to fit the above parametrized non-linear function to the processed creep data defined in the 'processed design data' section. In the second step, a

linear fitting of the parameters is performed to define a single analytical expression, which describes the creep behavior for any stress. Each of the five parameters can be represented as a linear function of the stress

$$K_0 = A_1 + B_1 R; \ K_1 = A_2 + B_2 R; \ b_1 = A_3 + B_3 R; \ K_2 = A_4 + B_4 R; \ b_2 = A_5 + B_5 R \quad (5)$$

Thus, for a given temperature this model can describe the three creep regimes and minimum creep rate for a range of stresses.

2.3.2. Neural Network Model (NN)

The neural network used in the model has a single hidden layer with n nodes (Figure 7).
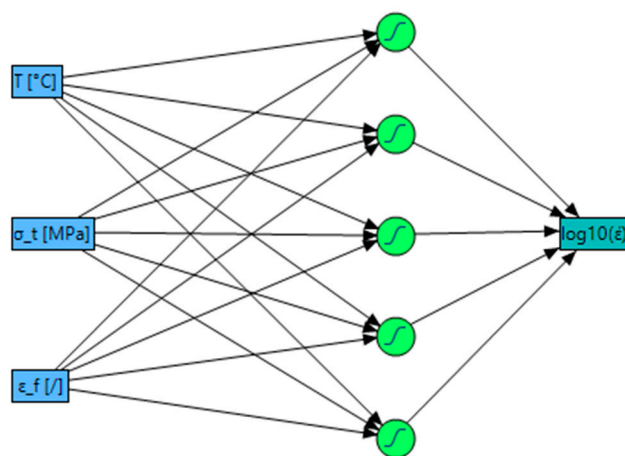

Figure 7. Diagram of the neural network with $n = 5$ nodes for the NN model.

Each node in the neural network uses a tanh type activation function. The argument of each activation function H_i is a linear combination of the independent variables

$$H_i(T, \sigma_t, \varepsilon_f) = \tanh\left\{0.5\left(h_{i,0} + h_{i,1}T + h_{i,2}\sigma_t + h_{i,3}\varepsilon_f\right)\right\} \quad (6)$$

The range of creep rates to be predicted spans several orders of magnitude (Figure 4). Trying to model $\dot{\varepsilon}_f$ directly leads to negative (un-physical) creep rates for some conditions where the creep rates are very small. It is therefore more convenient to work with logarithm of the creep rate rather than the creep rate itself.

The dependent variable $\log_{10}(\dot{\varepsilon}_f)$ for a neural network with n nodes in the hidden layer is expressed as a linear combination of the activation functions

$$\log_{10}(\dot{\varepsilon}_f) = k_0 + \sum_{i=1}^{n} k_i H_i(T, \sigma_t, \varepsilon_f) \quad (7)$$

where k_i are model parameters. The neural platform of the commercial software package JMP [25] was used for optimizing this model.

Figure 8 shows the evolution of *RMSE* (Root Mean Square Error) and the ratio *RMSE*(training)/*RMSE*(validation) for the training and the validation sets with n, the number of nodes in the hidden layer. Initially, both curves show a very quick improvement of the model performance with increasing n. However, increasing the nodes beyond five (dashed line) does not lead to further significant model improvements. The model with five nodes also has highest ratio *RMSE*(training)/*RMSE*(validation). Although further increasing the number of nodes to 10, for example, would slightly improve the RMSE, the accuracy with 5 nodes is sufficient given the finite accuracy of the underlying experimental data. Therefore, in this work a model with 5 nodes is used.
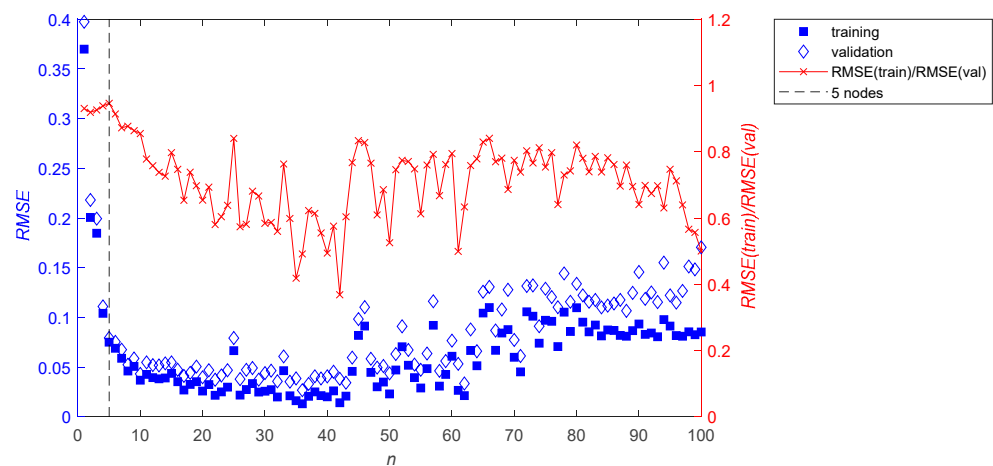
Figure 8. RMSE dependence on the number of nodes in the neural network. Note that $\log 10(\dot{\varepsilon}_f)$ is modeled rather than $\dot{\varepsilon}_f$.

It should be noted that the algorithm used for the optimization of the neural network uses randomized starting values for the fitting procedure, so different runs lead to different sets of model parameters. This though is of no concern given that the individual parameters in Equations (6) and (7) have no physical meaning. The general trends in Figure 8 are consistent between different runs.

2.3.3. Symbolic Regression Model (SR)

In this approach the dataset in the 'processed design data' section is modeled using the Eureqa software [26,27]. Eureqa is an artificial intelligence powered tool that builds analytical models to describe sets of data. This approach is fundamentally different from the method described in the previous section, although both methods are based on AI. In the NN model, a neural network fits the processed data with a mathematical expression that has a pre-defined form based on the hyperbolic tangent as activation function. The RS model is based on symbolic regression and genetic programming. Conventional regression methods fit parameters to an analytical expression of a given form (as in the case of the PA model) while symbolic regression searches both the form of the analytical expression and the parameters simultaneously. As explained by Schmidt and Lipson [26], the initial analytical expression is generated by randomly combining mathematical building blocks such as algebraic operators, analytical functions, variables and constants. New equations are formed by recombining previous equations and probabilistically modifying some parts. The genetic algorithm selects the expressions that better capture the data and discards the less accurate solutions, iterating the process on the selected expressions. The process continues until the desired level of accuracy is achieved.

3. Results

3.1. PA Model

It must be emphasized that in the second step of the two-step optimization procedure, the outcome of the automatic fitting has to be modified because the mathematical fitting provides un-physical values in the high stress region. In Figure 9, for temperature equal to 650 °C the initial fitting produces a dashed line with a strong negative slope (-1.9) that generates a negative K_0 for values of the stress that are larger than $-A_1/B_1 = 1540/1.9 = 810.5$ MPa. Since the scope of this work is to identify a creep expression that can be used also in other applications e.g., FEA simulations of small punch tests where the computed local stress can be larger than 810.5 MPa, the initial fitting is considered unsuitable. To describe creep phenomena for larger stress values, the negative slope is reduced by a factor 10 to -0.19. The fitting procedure has been repeated with the reduced slope and all other parameters have been recalculated accordingly. The new fit is

depicted as a continuous line in Figure 9. With the new parameters, the threshold stress above which K_0 becomes negative is much larger, $A_1/B_1 = 1159/0.19 = 6100$ MPa, which is a more acceptable value. A similar fitting procedure has been performed for the parameters for a temperature equal to 700 °C and 600 °C and the final outcome of the procedure for all parameters at all temperatures is included in Table 2, noting that Equations (4) and (5) with the Table 2 parameters provide the creep rate in 1/s.
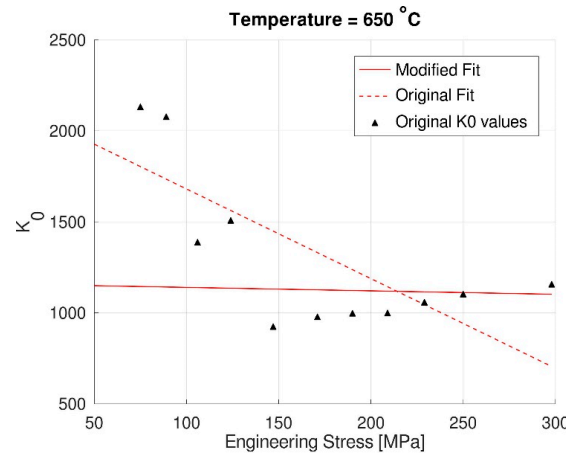

Figure 9. K_0 vs. engineering stress for $T = 650$ °C and fitting lines (Equation (5)).

Table 2. Values of the parameters for creep rate expression (1/s) in Equation (5).

T (°C)	A_1 (MPa)	B_1	A_2 (MPa)	B_2	A_3 (MPa)	B_3	A_4 (MPa)	B_4	A_5 (MPa)	B_5
700	1210	0	592	0	650	0	122	0	13	0
650	1159	−0.19	890	0.38	279	0.1	470	0.075	16.073	0
600	1855	0.1	939	0.2	319	0.1	500	0.725	16.75	0

The n_{Nort} value in Equation (4) is identified by fitting the minimum creep strain rate for each initial engineering stress as shown in Figure 10 for 650 °C, according to the Norton model in Equation (8)

$$\dot{\varepsilon}_{\mathrm{f}}(t) = \left\{ \frac{\sigma_t(t)}{K_{Nort}} \right\}^{n_{Nort}} \qquad (8)$$
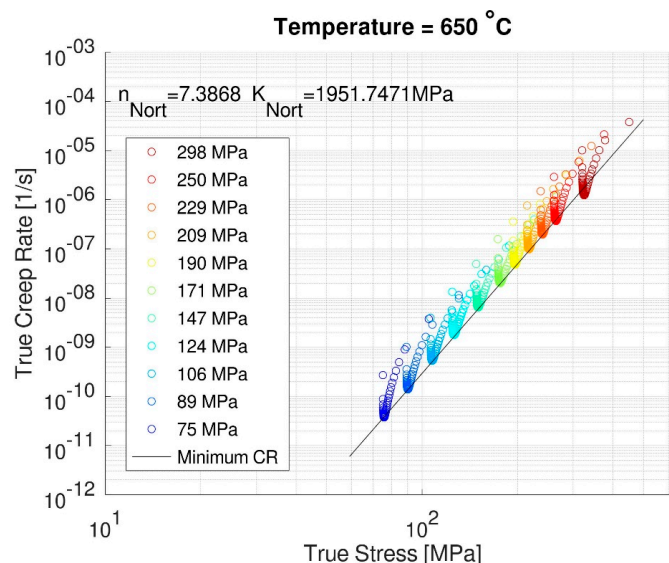

Figure 10. True creep rate vs. true stress for $T = 650$ °C and fitting line with minimum creep rate.

In Table 3, the values for the n_{Nort} and K_{Nort} are provided. The agreement between the LCSP processed true data and the model predictions is shown in Figures A1 and A2 in Appendix B.

Table 3. n_{Nort} and K_{Nort} for temperature equal to 700 °C, 650 °C, and 600 °C.

T (°C)	n_{Nort}	K_{Nort} (MPa)
700	6.4321	1778.5400
650	7.3868	1951.7471
600	7.7365	2771.0933

3.2. NN Model

The parameters in Equations (6) and (7) are included in Table 4.

Table 4. Coefficients for the NN-Model as defined in Equations (7) and (8) for the prediction of $\log_{10}(\dot{\varepsilon}_f)$.

| i	k_i	$h_{i,0}$	$h_{i,1}$ (1/°C)	$h_{i,2}$ (1/MPa)	$h_{i,3}$ (-)
0	-32.0496653	-	-	-	-
1	-70.7655528	1.79858370	-0.0107120662	0.00135983393	-10.1628092
2	116.453727	-1.68672486	-0.004602022777	-0.00157195945	-309.465775
3	19.2339490	-3.86265632	0.00812758304	0.0158607961	0.951844841
4	-56.1634224	-641.682543	0.912286145	-0.0316191609	-240.521332
5	1.66841774	-14.9047381	0.0183251616	0.0145318325	-2.13261636

Figure 11a,b compares the performance of the NN-Model for describing $\dot{\varepsilon}_f$ for the training and validation sets. The root mean squared relative error (*RMSRE*)

$$RMSRE = \sqrt{\frac{1}{N}\sum_{i=1}^{N}\left|\frac{a_{vi} - p_{vi}}{a_{vi}}\right|^2} \tag{9}$$

is added to the plots to provide a quantification of the difference between the model predicted values p_{vi} and the actual values a_{vi} (LCSP processed data). Zero would indicate a perfect fit to the data. Note that this comparison is for $\dot{\varepsilon}_f$, the actual quantity of interest, rather than $\log_{10}(\dot{\varepsilon}_f)$ as was used for the model optimization. The model performance is therefore not as good as might be expected from Figure 8.

RMSRE indicates a better performance for the validation than for the training set, demonstrating that the model does not over-fit the data. In Figure 11c and in Figure 11d the relative residuals are shown for the training set and the validation set respectively (i.e., the relative residual is the difference between the actual and the predicted value divided by the actual value). For a good model, there should not be any trends in the residuals. The range of scatter for both sets is quite similar and there is no discernible trend in either plot. This demonstrates that the model performs equally well over the entire range, $\dot{\varepsilon}_f$.

The agreement between the LCSP processed true data and the model predictions is shown in Figures A3 and A4 in Appendix B.
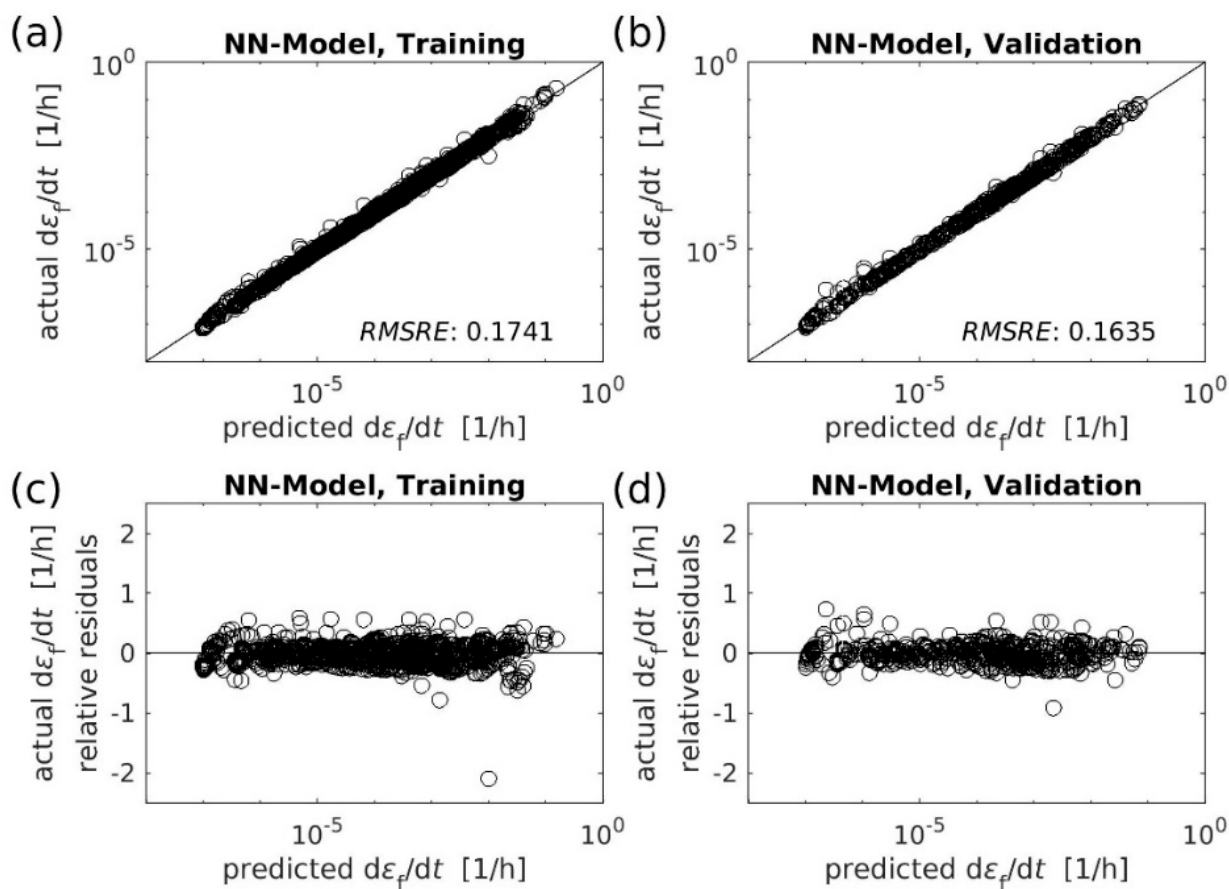
Figure 11. NN-Model. Actual vs. predicted plot for the training data-set (**a**) and the validation data-set (**b**). Relative residuals for the training data-set (**c**) and the validation data-set (**d**).

3.3. SR Model

The initial dataset as defined in the 'processed design data' section has been divided in the exact same way as for the NN-Model: the same two thirds of the dataset were used as training data and the remaining third as validation data. The creep rate has been expressed as function of true stress, temperature, and the natural logarithm of creep strain plus one. A value of one is added to the creep strain to avoid computing a logarithm of zero (when the creep strain is zero).

The creep rate expression (1/h) with the stress in MPa is (model parameters g_i are listed in Table 5)

$$\dot{\varepsilon}_f(t) = exp\left\{ g_1 - \frac{g_2}{T} + g_3 \left[ln\left(\varepsilon_f + 1\right) \right]^{0.5} + g_4\, \sigma_t^{0.5} - g_5 ln\left(\varepsilon_f + 1\right) - g_6 T \sigma_t - g_7 T \left[ln\left(\varepsilon_f + 1\right) \right]^{g_8} \right\} \tag{10}$$

Table 5. Parameters for Equation (10).

g_1	g_2	g_3	g_4	g_5	g_6	g_7	g_8
3.8715858×10^1	4.203906578×10^4	6.0373303×10^1	2.608310	3.6754558×10^1	8.612516×10^{-5}	5.653715×10^{-2}	2.13110×10^{-1}

The *RMSRE* values for the validation set and for the training set are close, indicating that over-fitting is not occurring in the model as shown in Figure 12. Also for this model, as for the NN model, in the relative residuals shown in Figure 12c,d, the data scattering is similar in the training and validation sets without apparent trends, showing that the model performance is satisfactory over the whole range of the creep rate. The agreement between the LCSP processed true data and the model predictions is shown in Figures A5 and A6 in Appendix B.
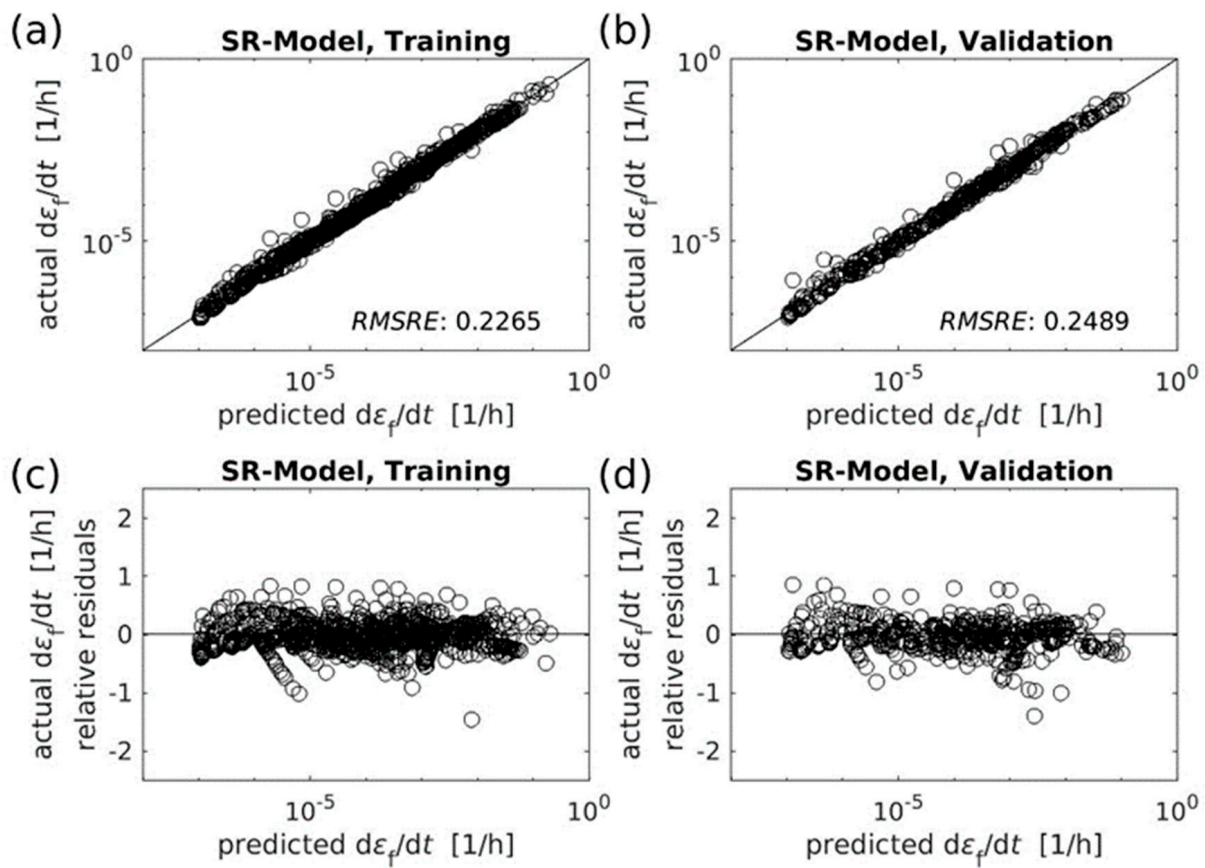
Figure 12. RS-Model. Actual vs. predicted plot for the training dataset (**a**) and the validation dataset (**b**). Relative residuals for the training dataset (**c**) and the validation dataset (**d**).

4. Discussion

For the comparison of the performance of the three models, the geometric mean bias (*GMB*) and the geometric mean variance (*GMV*) were selected as statistical indicators. The model performance is based on the model capacity of accurately reproducing the processed data. *GMB* and *GMV* provide a complete and compact way to assess the model performance and they are particularly suitable for datasets where the variables vary by many orders of magnitude, as in the present case [28]

$$GMB = exp\left[\overline{ln\left(\frac{a_v}{p_v}\right)}\right] \quad GMV = exp\overline{\left[ln\left(\frac{a_v}{p_v}\right)\right]^2} \tag{11}$$

where a_v and p_v are the actual values (processed data) and the model predicted values respectively; the overline is the arithmetic mean. The Geometric Mean Bias measures the relative mean bias, which represents only the systematic error. In a perfect model *GMB* = 1, whereas *GMB* > 1 indicates a systematic under-prediction of the model and *GMB* < 1 a systematic over-prediction. A factor of two in the mean corresponds to *GMB* = 2 in case of under-prediction or 0.5 in case of over-prediction. The geometric mean variance measures the relative scatter and includes both the systematic and the random error. For the perfect model *GMV* = 1 and a value of about 1.6 for *GMV* indicates a factor of two for the scatter.

In Figure 13, *GMB* and *GMV* are shown for the three models. The parabola indicates the minimum *GMV* value for a given *GMB*. For each model, the statistical indicators for the training dataset, for the validation dataset, and for the complete dataset (i.e., the combined training and validation sets), have very similar values, and that is a further indication that the optimization processes were properly performed—e.g., no overfitting occurred. *GMB* is about 1 for the NN and SR model, indicating the absence of systematic error in

the models. For the PA model, $GMB \approx$ s1.13 indicates a slight tendency to a systematic under-prediction. GMV is equal to about 1.03, 1.07, and 1.12 for the NN, RS, and PA model respectively. The statistical analysis shows that the most accurate model in term of better fitting to the LCSP processed data is the NN model, followed by the RS model and then the PA model. However, all the three models show a good accuracy, as demonstrated by the small value of the statistical indicators.
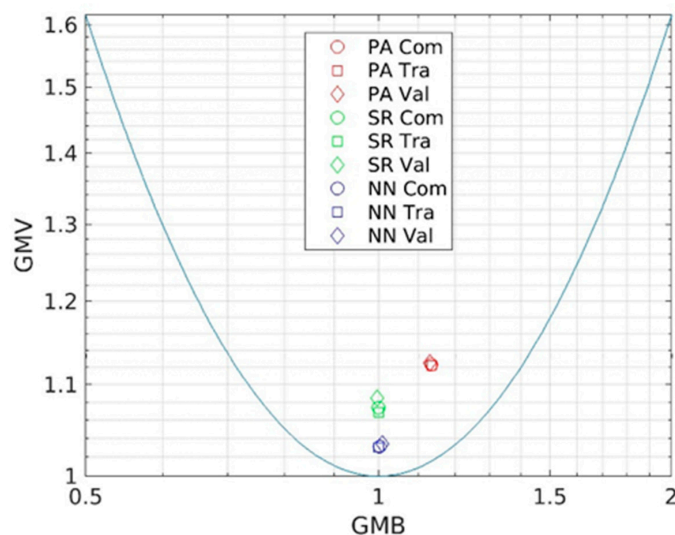
Figure 13. Geometric mean bias vs. geometric mean variance for the training (Tra), validation (Val), and complete (Com) dataset of the creep models.

In the PA model, three expressions are provided for the fixed temperatures of 600 °C, 650 °C, and 700 °C while the in the NN and RS model, there is only one general expression which can be applied for any temperature between 600 °C and 700 °C.

Another advantage of the NN and SR model compared to the PA model is the fact that they can be developed with an automatic procedure while the PA model requires two steps and the second step is not completely automatic if unphysical values are generated like in this investigation. Therefore, the procedure for the PA model development is more complicated and time-consuming.

On the other hand, the PA model is the only model with a pre-defined form that is based on the phenomenological dependence of the creep rate on the true stress and true creep strain and where the primary, secondary, and tertiary regime can be identified easily. The physics of the creep phenomena cannot be identified in the expression of the NN model. Compared to the NN model, in principle in the SR model it is easier to relate the mathematical expression to the physics of the phenomena and to perform the analysis of the contribution of the different terms to the creep rate, helping to reveal the physics underlying the observed phenomena. However, a complete analysis of this type goes beyond the scope of this paper.

A set of experiments from the literature was used for the comparison between the simulation results and measurement data. The uni-axial creep experiments were performed for the following conditions: the engineering stress equal to 300, 280, 260, 240, 220, 200, 180, and 150 MPa at 600 °C; the engineering stress equal to 240, 200, 160, 140, 120, and 100 MPa at 650 °C; and the engineering stress equal to 170, 150, 120, 100, and 80 MPa at 700 °C [16].

For the same conditions of temperature and stress, FE simulations of creep tests on uniaxial specimens have been performed with the Abaqus code [29] and the Z-mat material library [30]. Z-mat provides a collection of constitutive models and can easily be extended with new models. In this case, the constitutive tensile model from Equation (2) as the time-independent component has been combined in the Z-mat input file with the creep rate models (from Equations (4), (6), and (10)) as the visco-plastic component.

In Figures 14 and 15, the comparison between the LCSP engineering processed data, the experimental measurements and the simulation results from the FE analysis are shown for 650 °C. The following considerations are valid also for 700 °C and 600 °C as shown in Figures A7 and A8 in Appendix C, noting that the engineering stresses for LCSP are those that can be found in the rupture strength table of the RCC-MRx code i.e., they are different from the engineering stresses in the FZK experiments shown in the figures.
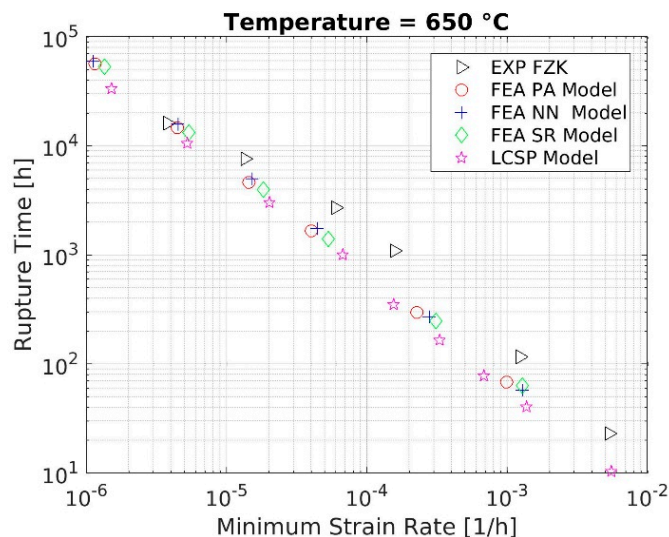

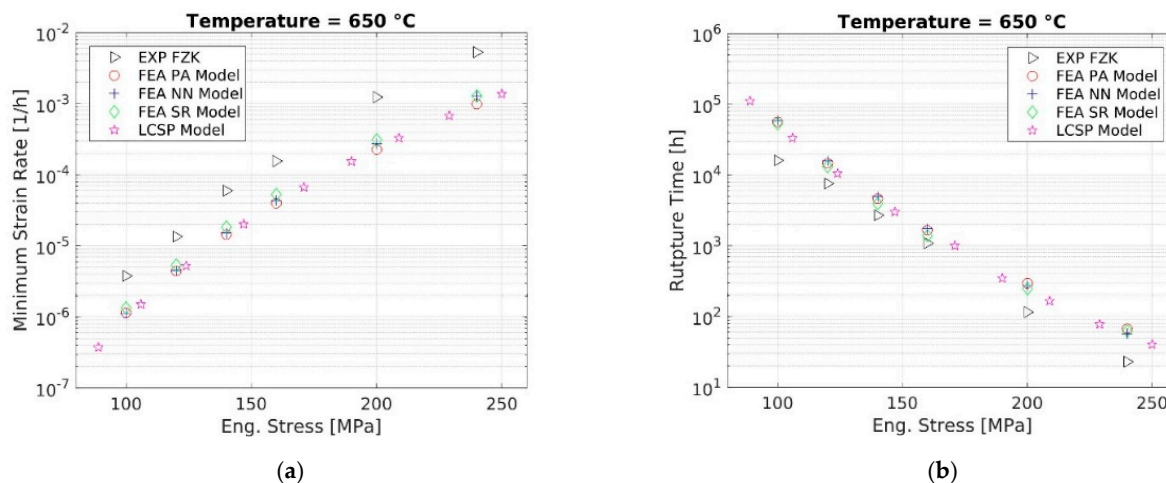**Figure 14.** Rupture time vs. minimum strain rate.

Figure 15. For 650 °C, (**a**) minimum strain rate vs. initial engineering stress, (**b**) rupture time vs. engineering stress.

The LCSP processed data have been used for the development of the creep rate models. Therefore, the results from the FEA simulations are in good agreement among themselves (Figure 15). Moreover, a good level of agreement between the LCSP data and the creep models is demonstrated in the same figure.

The FZK experimental rupture times are shorter than LCSP values, and consistently the minimum strain rate is larger in the FZK experiments than in the LCSP data. It is known that different batches of the same material can have different properties within a certain range. For this reason, in RCC-MRx the rupture times are provided both for an average value of the rupture stress and for a minimum value. The LCSP processed data are based on the average RCC-MRx data and the discrepancy between the LCSP data and the FZK indicates that the average RCC-MRx material is stronger than the material in the FZK experiments. FZK measurements of rupture times lay between the average and minimum

RCC-MRx values. Therefore, the 316L(N) in the FZK experiments can be considered as a specific case at the lower end of the range of materials whose data were included in the RCC-MRx code. However, the results of the FEA simulations show the same qualitative trends as the FZK measurements.

It must be noted that the optimization of the A_i and B_i parameters in Equation (5) of the PA model is performed for the engineering stress as shown in Section 3.1. For simulations of uni-axial tests, the value of the engineering stress is known, so in principle one could use Equation (5) with the engineering stress in the calculations. However, for other tests such as the small punch tests, the engineering stress is not known and the calculation provides the true stress. Therefore, it is assumed that the true stress could be used in Equation (5) in the application of the model, although using the engineering stress would be more consistent. The assumption of using the engineering stress in the second step of the optimization procedure and the true stresses in the application of the derived creep model is justified as follows:

- As shown in Table 2, for the 700 °C all B_i are zero, and therefore there is no dependence of Equation (5) on the stress and there is no effect of the assumption. For the 650 °C, the B_i are zero or very small, causing a weak dependence on the stress, as shown in Figure 9, where K_0 is almost constant for a wide range of stress. Also, for the 600 °C, the situation is similar for most of the B_i although B_4 has a larger value.
- In Appendix D (Table A2) the ratio of the minimum strain rates and the ratio of the rupture times for the simulation results with the true values and the engineering values of the stress in Equation (5). Those ratios show a maximum difference of 1% for the minimum strain rates and 2% for the rupture times. The ratios values for the 700 °C are not shown because they are equal to 1.

5. Conclusions

By means of the LCSP model, the RCC-MRx data and analytical expressions were used to generate processed engineering data for the primary, secondary and tertiary creep stages of 316L(N) steel over a wide range of engineering stress (57–315 MPa) and for three temperatures (600 °C, 650 °C, 700 °C). The engineering data were converted to true values and used to develop three models for the true creep rate:

- PA model: a phenomenological model with a predefined form of the function based on the Norton law,
- NN model: a model based on neural network using the hyperbolic tangent as activation function; the model is a linear combination of terms with a pre-defined form
- SR model: a model based on artificial intelligence, which searches for an analytical expression and related parameters by symbolic regression.

FE simulations show that all three models are capable of reproducing the minimum creep strain and the rupture times of the LCSP processed data over a wide range of temperatures and engineering stresses. The statistical analysis of the model's performance shows that the NN model is the most accurate for the 316L(N) material. However, the statistical indicators show a satisfactory accuracy also for the other 2 models.

The models were developed with the RCC-MRx average material properties. It is known that for different batches of the same material, the material properties can be significantly different. In that case, depending on the required level of accuracy, it might be necessary to recalibrate the model parameters.

Furthermore, it is shown that the results from the FE simulations based on the creep models are also in good qualitative agreement with experimental data from the literature, capturing the same trends as the experiments. From the quantitative point of view, it must be emphasized that the average minimum creep rate and the rupture times in the RCC-MRx code (and consequently for the creep models based on RCC-MRx) are for a higher strength batch of material than in the experiments.

In all three models, the true creep rate is expressed as a function of true stress and true creep strain, which can be used as inputs for the creep material properties in FE

codes to perform simulations for the investigation of creep phenomena for an "average" 316L(N) material.

Author Contributions: Conceptualization, S.H. and K.-F.N.; Formal analysis, D.B., S.H. and M.B.; Investigation, D.B. and S.H.; Methodology, D.B., S.H., K.-F.N. and M.B.; Project administration, I.S.; Software, D.B., M.B. and I.S.; Supervision, K.-F.N.; Validation, D.B., S.H. and M.B.; Visualization, D.B. and M.B.; Writing—original draft, D.B., S.H., K.-F.N. and M.B.; Writing—review and editing, D.B., S.H., K.-F.N., M.B. and I.S. All authors have read and agreed to the published version of the manuscript.

Conflicts of Interest: The authors declare no conflict of interest.

Nomenclature

|	
A_g	uniform elongation
a_v	actual values
b_i	fitting parameters, Equation (4)
E	Young's modulus
e_t	engineering total strain (/);
e_{ffp}	average eng. strain at the end of primary creep (/); ε_{ffp} in RCC-MRx
$\dot{e}_{fp}$	average eng. creep strain rate for primary creep (1/h); $\dot{\varepsilon}_f$ in RCC-MRx
$\dot{e}_{fs}$	average eng. strain rate for secondary creep (1/h); $\dot{\varepsilon}_s$ in RCC-MRx
g_i	parameters in Equation (10)
GMB	Geometric Mean Bias
GMV	Geometric Mean Variance
H_i	activation function in neural network
$h_{i,j}$	coefficients in activation function H_i
k_i	coefficients in neural network model
K_i, A_i, B_i	fitting parameters in Equation (5)
n	number of nodes in the hidden layer of the neural network
n_{Nort}, K_{Nort}	exponent and denominator in Norton law—Equation (8)
p_v	model predicted values
$P_{R0}, P_H, P_{Q1}, P_{Q2}, P_{b1},$ and P_{b2}	fitting parameters in Equation (2) for tensile properties
R	engineering stress (MPa)
R_0	Initial engineering stress (MPa)—applied force divided by the original cross-section area of the test sample
$RSMRE$	Root Square Mean Relative Error
T	temperature (°C)
t	time (h)
t_u	Time to rupture for a test piece maintained at specified T and initial stress R_0 (h)
t_{fp}	RCC-MRx average end of the primary creep time (h)
$x_0, p,$ and C	fitting parameters in LCSP model—Equation (3)
ε_t	true total strain (/)
ε_e	true elastic strain (/)
ε_p	true plastic strain (/)
ε_f	true creep strain (/)
$\dot{\varepsilon}_f$	true creep strain rate (1/h)
σ_t	true stress (MPa)

Appendix A. LCSP Model Parameters

$C = 4.0$ for all cases.

Table A1. Parameters x_0 and p of the LCSP model at 600 °C (top), at 650 °C (middle), and at 700 °C (bottom).

T = 600 °C											
R_0 (MPa)	351	316	300	284	263	245	214	184	160	137	118
x_0	−2.884	−2.959	−2.986	−3.010	−3.036	−3.086	−3.131	−3.151	−3.137	−3.076	−2.942
p	4.308	4.534	4.592	4.643	4.763	4.159	4.275	4.503	4.831	5.395	6.484
T = 650 °C											
R_0 (MPa)	298	250	229	209	190	171	147	124	106	89	75
x_0	−2.799	−2.945	−3.015	−3.082	−3.151	−3.228	−3.331	−3.432	−3.512	−3.569	−3.573
p	3.962	3.818	3.788	3.699	3.651	3.417	3.440	3.474	3.521	3.684	4.015
T = 700 °C											
R_0 (MPa)	257	213	195	165	140	117	99	82	69	57	47
x_0	−2.581	−2.836	−2.896	−3.071	−3.245	−3.433	−3.616	−3.827	−4.022	−4.229	−4.429
p	3.224	3.227	3.015	2.881	2.778	2.675	2.621	2.604	2.631	2.665	2.720

Appendix B. Comparison between Model Predicted Values and Processed Design Data
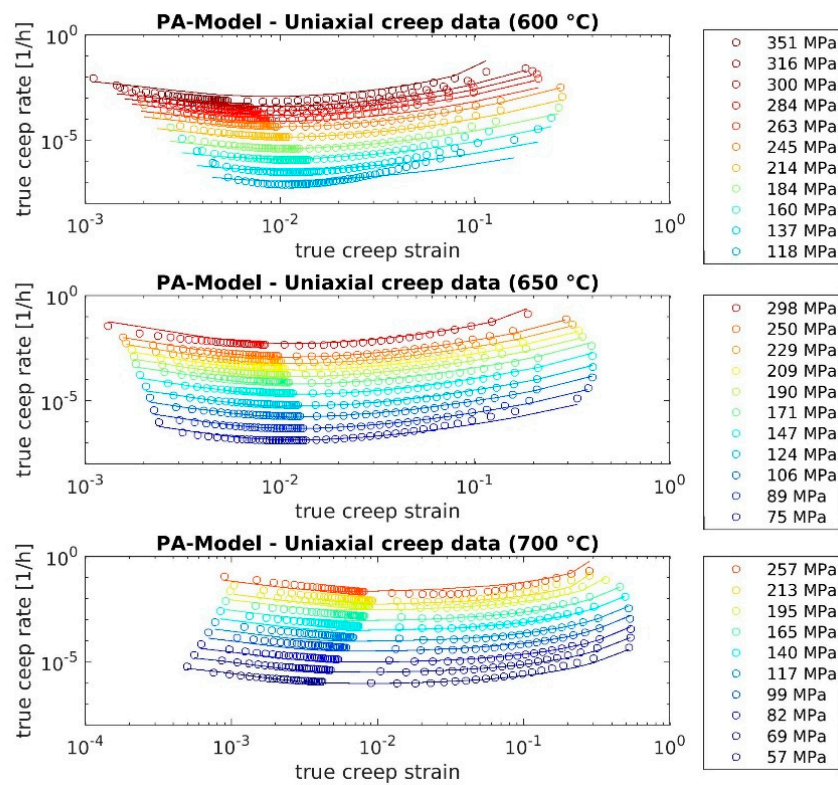
Figure A1. PA model: true creep rate vs. true creep strain for 600 °C, 650 °C, and 700 °C. Predicted values (lines) and processed design values (dots).
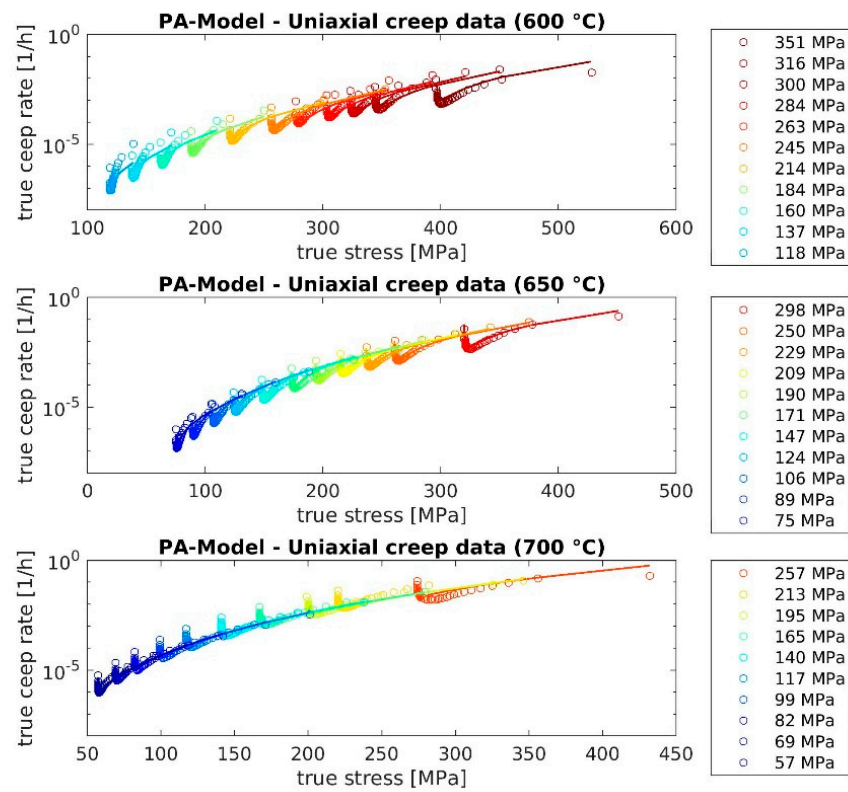
Figure A2. PA model: true creep rate vs. true stress for 600 °C, 650 °C, and 700 °C. Predicted values (lines) and processed design values (dots).
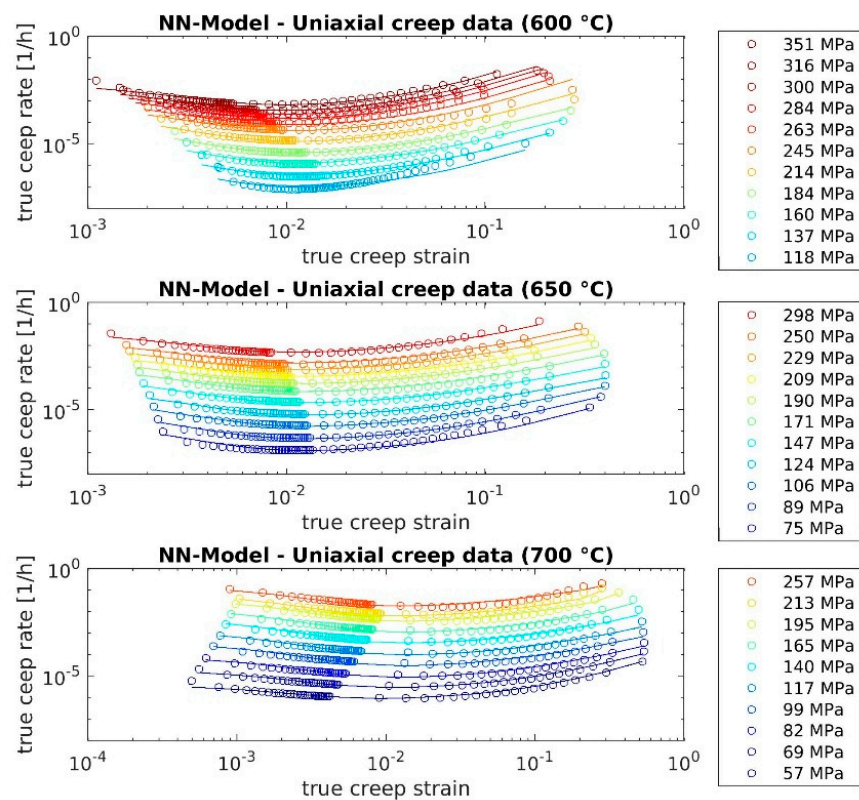

Figure A3. NN model: true creep rate vs. true creep strain for 600 °C, 650 °C, and 700 °C. Predicted values (lines) and processed design values (dots).
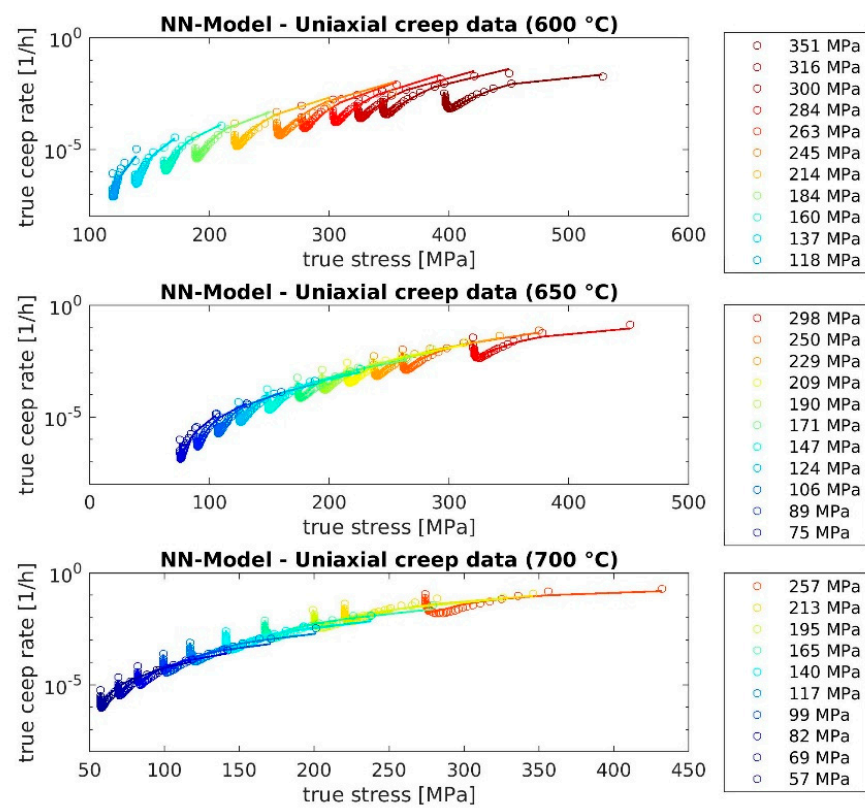
Figure A4. NN model: true creep rate vs. true stress for 600 °C, 650 °C, and 700 °C. Predicted values (lines) and processed design values (dots).
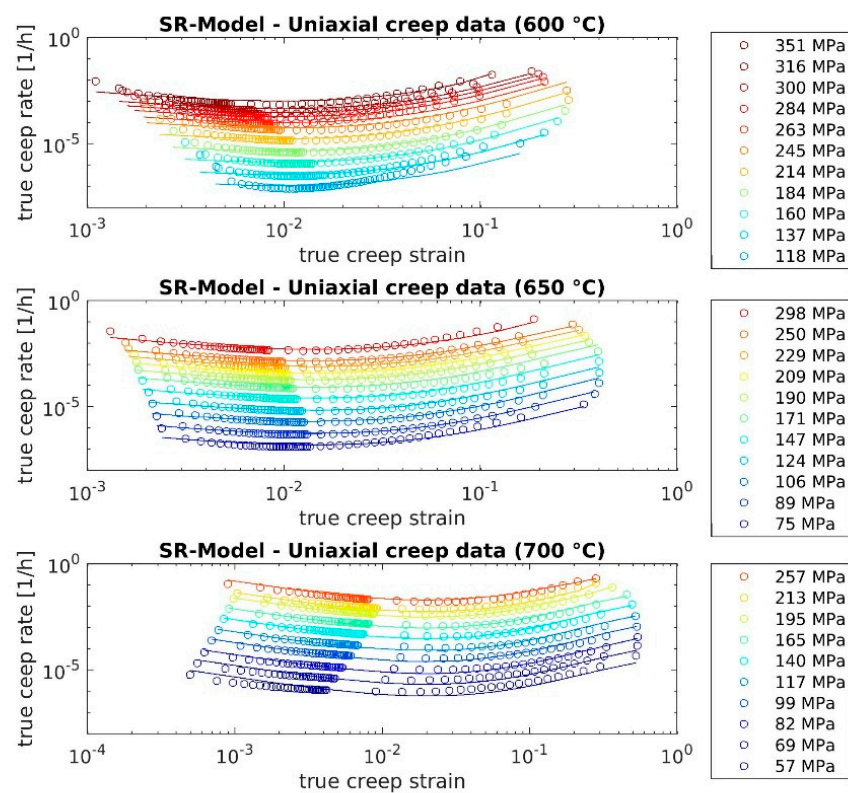

Figure A5. SR model: true creep rate vs. true creep strain for 600 °C, 650 °C, and 700 °C. Predicted values (lines) and processed design values (dots).
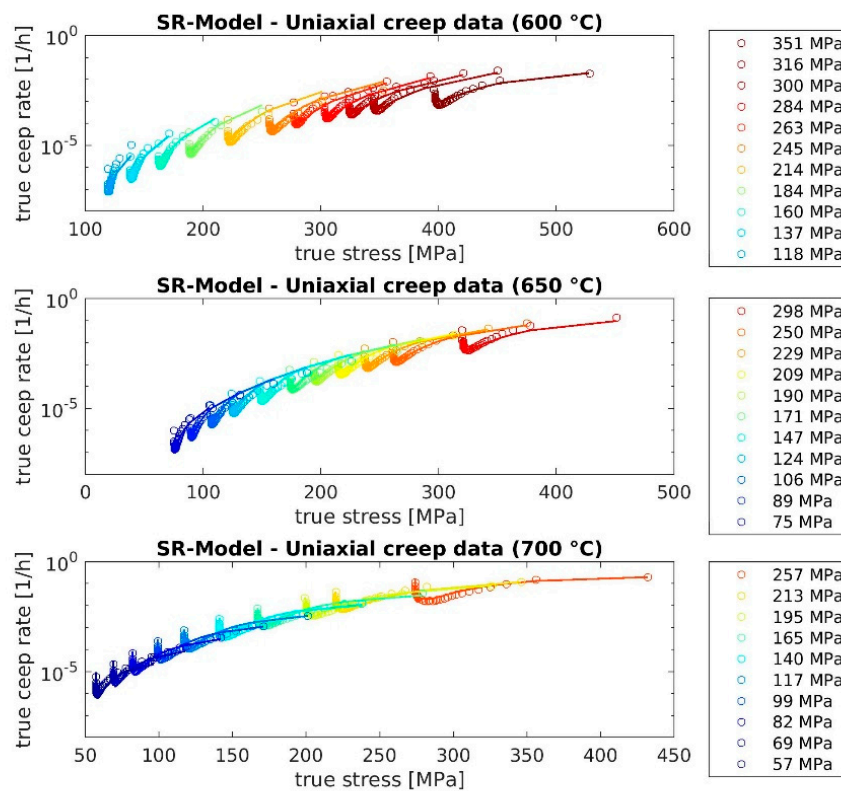
Figure A6. SR model: true creep rate vs. true stress for 600 °C, 650 °C, and 700 °C. Predicted values (lines) and processed design values (dots).

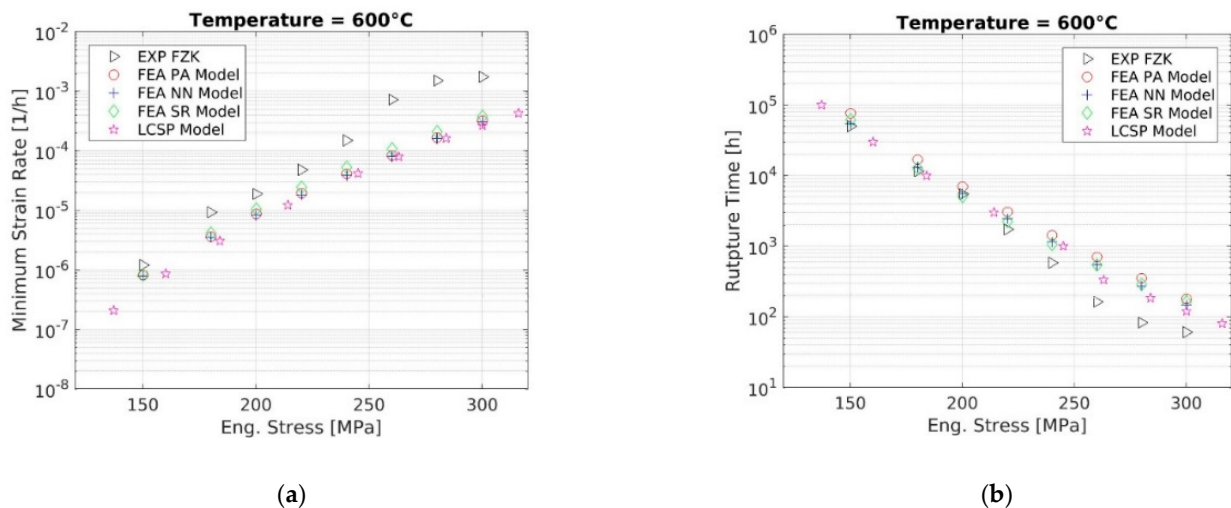## Appendix C. Rupture Times and Minimum Strain Rate for the PA Model

(**a**)

(**b**)

Figure A7. For 600 °C, (**a**) minimum strain rate vs. initial engineering stress, (**b**) rupture time vs. engineering stress.
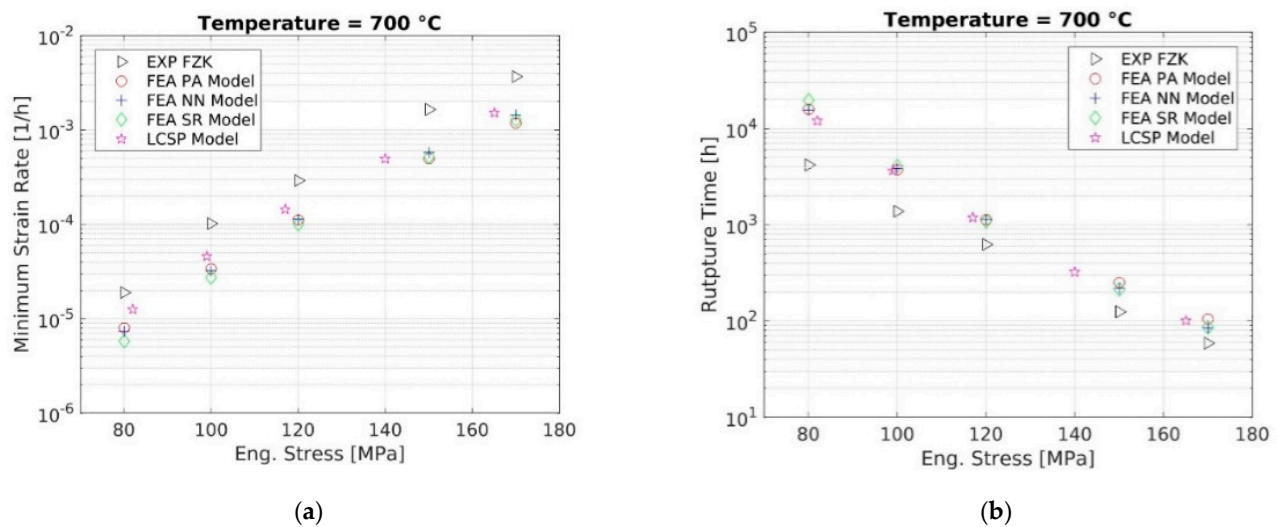
Figure A8. For 700 °C, (**a**) minimum strain rate vs. initial engineering stress, (**b**) rupture time vs. engineering stress.

Appendix D. Rupture Times and Minimum Strain Rate for the PA Model

Table A2. Minimum strain rate and rupture times from the FEA simulations.

T (°C)	Eng Stress (MPa)	MinStrainRate_A	t_u_A (h)	MinStrainRate_B	t_u_B (h)	Ratio 1	Ratio 2
650	240	9.90×10^{-4}	67.95	9.99×10^{-4}	66.79	1.01	0.98
650	200	2.27×10^{-4}	295.79	2.29×10^{-4}	291.93	1.01	0.99
650	160	4.00×10^{-5}	1667.71	4.00×10^{-5}	1651.7	1.00	0.99
650	140	1.44×10^{-5}	4611.83	1.44×10^{-5}	4574.72	1.00	0.99
650	120	4.44×10^{-6}	14,700.16	4.45×10^{-6}	14,602.07	1.00	0.99
650	100	1.15×10^{-6}	56,523.94	1.16×10^{-6}	56,208.72	1.01	0.99
600	300	3.24×10^{-4}	180.32	3.24×10^{-4}	183.58	1.00	1.02
600	280	1.66×10^{-4}	352.27	1.68×10^{-4}	359.4	1.01	1.02
600	260	8.37×10^{-5}	701.24	8.46×10^{-5}	715.6	1.01	1.02
600	240	4.12×10^{-5}	1438.14	4.16×10^{-5}	1467.78	1.01	1.02
600	220	1.95×10^{-5}	3077.77	1.96×10^{-5}	3138.05	1.01	1.02
600	200	8.69×10^{-6}	6960.54	8.73×10^{-6}	7088.76	1.00	1.02
600	180	3.62×10^{-6}	16,893.6	3.63×10^{-6}	17,180.17	1.00	1.02
600	150	8.15×10^{-7}	76,271.78	8.17×10^{-7}	77,376.39	1.00	1.01

References

1. Holdsworth, S.R. Constitutive equations for creep curves and predicting service life. In *Creep Resistant Steels*; Abe, F., Kern, T.-U., Viswanathan, R., Eds.; CRC Press Woodhead Publishing Limited: Cambridge, UK, 2008; pp. 403–420.
2. Granacher, J.; Möhlig, H.; Schwienheer, M.; Berger, C. Creep equation for high temperature material. In Proceedings of the 7th International Conference on Creep & Fatigue at Elevated Temperatures (Creep 7), Tsukuba, Japan, 3–8 June 2001; pp. 609–616.
3. Merckling, G. Metodi di calcolo a confronto per la previsione dellulteriore esercibilità in regime di scorrimento viscoso. In Proceedings of the Conference on Fitness for Service, Giornata di Studio CESI-CONCERT, Milan, Italy, 28 November 2002.
4. Esposito, L.; Bonora, N.; De Vita, G. Creep modelling of 316H stainless steel over a wide range of stress. *Struct. Integr. Procedia* **2016**, *2*, 927–933.
5. Praveen, C.; Christopher, J.; Ganesan, V.; Prasad Reddy, G.V.; Sasikalaa, G.; Albert, S.K. Constitutive modelling of transient and steady state creep behaviour of type 316LN austenitic stainless steel. *Mech. Mater.* **2019**, *137*, 103–122. [CrossRef]
6. Praveen, C.; Christopher, J.; Ganesan, V.; Prasad Reddy, G.V.; Albert, S.K. Influence of varying nitrogen on creep deformation behaviour of 316LN austenitic stainless steel in the framework of the state-variable approach. *Mater. Sci. Eng. A* **2021**, *803*, 1–13. [CrossRef]
7. RCC-MRx. *Design and Construction Rules for Mechanical Components of Nuclear Installations: High Temperature, Research and Fusion Reactors*, Afcen RCC-MRx Code 2018 Edition ed; Afcen: Courbevoie, France, 2018.
8. Tavassoli, A.-A. 16-8-2 weld metal design data for 316L(N) steel. *Fusion Eng. Des.* **2008**, *83*, 1467–1470. [CrossRef]

9. Lebarbé, T.; Marie, S.; Drubay, B.; Gelineau, O.; Bonne, D.; De La Burgade, F. Presentation of the Afcen RCC-MRx Code for Sodium Reactors (SFR), Research Reactor (RR) and Fusion (ITER): General Overview. In Proceedings of the ASME 2010 Pressure Vessels and Piping Division/K-PVP Conference. ASME 2010 Pressure Vessels and Piping Conference, Bellevue, WA, USA, 18–22 July 2010; Volume 1, pp. 797–802.
10. Lee, H.-Y. Comparison of elevated temperature design codes of ASME Subsection NH and RCC-MRx. *Nucl. Eng. Des.* **2016**, *308*, 142–153. [CrossRef]
11. Pétesch, C.; Lebarbé, T.; Gelineau, O.; Vallot, D.; Blat-Yrieix, M. 2018 RCC-MRX Code Edition: Context, Overview, On-Going Developments. In Proceedings of the ASME 2018 Pressure Vessels and Piping Conference. Codes and Standards, Prague, Czech Republic, 15–20 July 2018; pp. 1018–1026.
12. Muñoz Garcia, J.E.; Petesch, C.; Lebarbé, T.; Pascal, C.; Bonne, D.; Vallot, D.; Gelineau, O.; Blat, M. Design and construction rules for mechanical components of high-temperature, experimental and fusion nuclear installations: The RCC-MRX code last edition. In Proceedings of the International Conference on Nuclear Engineering, Proceedings, ICONE27, Ibaraki, Japan, 19–24 May 2019.
13. Holmström, S.; Auerkari, P. Robust prediction of full creep curves from minimal data and time to rupture model. *Energy Mater. Mater. Sci. Eng. Energy Syst.* **2006**, *1*, 249–255. [CrossRef]
14. Holmström, S.; Auerkari, P. Predicting creep rupture from early strain data. *Mater. Sci. Eng. A* **2009**, *510*, 25–28. [CrossRef]
15. Holmström, S. Engineering Tools for Robust Creep Modeling. VTT Publications. Doctoral Thesis, Aalto University, Espoo, Finland, 2010.
16. Rieth, M.; Falkenstein, A.; Graf, P.; Heger, S.; Jaentsch, U.; Klimiankou, M.; Materna-Morris, E.; Zimmermann, H. *Creep of the Austenitic Steel AISI 316L(N). Experiments and Models*; FZKA 7065 Report; Forschungszentrum Karlsruhe GmbH: Karlsruhe, Germany, 2004.
17. Larson, F.R.; Miller, J. Time-Temperature Relationship for Rupture and Creep Stresses. *Trans. ASME* **1952**, *74*, 765–771.
18. Holmström, S.; Laukkanen, A.; Andersson, T. Creep Life Simulations of EB Welded Copper Overpack. *POSIVA Work. Rep.* **2012**, *96*.
19. Pohja, R. LCSP Creep Strain Model Performance of Zirconium Based Fuel Cladding Materials in Steady State and Transient Creep Conditions. *Tech. Rep.* **2016**. [CrossRef]
20. Kalyanasundaram, V. Creep, Fatigue and Creep-Fatigue Interactions in Modified 9% Cr–1% Mo (P91) Steels. Theses and Dissertations, University of Arkansas, Fayetteville, AR, USA, 2013.
21. Storesund, J.; Steingrimsdotter, K.; Rantala, J.; Sollander, R.; Zhouwang, C.; Bolinder, T. *Life Time of High Temperature Piping by Stress Analysis and Testing*; Energiforsk REPORT: Stockholm, Sweden, 2015; Volume 187, ISBN 978-91-7673-187-1.
22. Mohrmann, R.; Oesterlin, H. Residual Lifetime Estimation by Scatter Band Analysis of an E911 Pipe Bend of an USC Power Plant. In Proceedings of the 45th MPA-Seminar, Stuttgart, Germany, 1–2 October 2019.
23. Srinivasan, V.S.; Valsan, M.; Bhanu Sankara Rao, K.; Mannan, S.L.; Raj, B. Low cycle fatigue and creep–fatigue interaction behavior of 316L(N) stainless steel and life prediction by artificial neural network approach. *Int. J. Fatigue* **2003**, *25*, 1327–1338. [CrossRef]
24. Srinivasan, V.S.; Choudhary, B.K.; Mathew, M.D.; Jayakumar, T. Long-term creep-rupture strength prediction for modified 9Cr–1Mo ferritic steel and type 316L(N) austenitic stainless steel. *Mater. High Temp.* **2012**, *29*, 41–48. [CrossRef]
25. JMP Software. Available online: https://www.jmp.com (accessed on 4 February 2019).
26. Schmidt, M.; Lipson, H. Distilling free-form natural laws from experimental data. *Science* **2009**, *324*, 81–85. [CrossRef] [PubMed]
27. Schmidt, M.; Lipson, H. Eureqa (Version 1.24) [Software]. Available online: www.nutonian.com (accessed on 28 January 2019).
28. Baraldi, D.; Melideo, D.; Kotchourko, A.; Ren, K.; Yanez, J.; Jedicke, O.; Giannissi, S.G.; Tolias, I.C.; Venetsanos, A.G.; Keenan, J.; et al. Development of a Model Evaluation Protocol for CFD Analysis of Hydrogen Safety Issues the SUSANA Project. *Int. J. Hydrog. Energy* **2017**, *42*, 7633–7643. [CrossRef]
29. Abaqus Software. Available online: https://www.3ds.com/products-services/simulia/products/abaqus/ (accessed on 10 January 2019).
30. Zmat Material Model Library Software. Available online: http://www.zset-software.com/products/z-mat/ (accessed on 10 January 2019).